



OPEN

Imaging LNAPL distribution at a former chemical plant with time-domain induced polarization

Yanhui Dong^{1,2}, Teng Xia³✉, Jian Meng⁴ & Deqiang Mao⁴✉

Light non-aqueous phase liquids (LNAPLs) that infiltrate into the subsurface are commonly described in two distinct zones: the source zone and the plume zone. A precise differentiation between these zones is essential for constraining further migration and selecting an effective remediation method. In this study, we employ the induced polarization (IP) method to characterize the contaminants. Six time domain IP survey lines were conducted at a former chemical plant contaminated with LNAPLs. Even though the contaminated areas corresponding to BTEX concentration above 180 mg/kg are less than 5 mS/m, the source and plume zones cannot be distinguished by conductivity alone. However, a noticeable difference in phase (φ) between the two zones is observed, and the threshold phase value corresponding to a critical concentration of 450 mg/kg is 20 mrad. Moreover, the normalized chargeability (M_n) threshold for the source zone is 80 mS/m, and the corresponding M_n differences between the source and plume zones are more significant than those in φ . These results illustrate that changes in polarization characteristics associated with BTEX concentrations can aid in further distinguishing between the source and plume zones. Ultimately, it is concluded that IP imaging is a well-suited method for LNAPL investigations that permits an improved characterization of different contaminated zones, which can facilitate the optimization of drillings for further site assessment and remediation.

Non-aqueous phase liquids (NAPLs) exhibit low solubility in water and are characterized by complex migration modes in heterogeneous aquifers. NAPLs can be divided into two categories: light non-aqueous phase liquids (LNAPLs), e.g., BTEX group, and dense non-aqueous phase liquids (DNAPLs), e.g., halohydrocarbon. These liquids are widely applied in industrial and chemical processes, but can pose serious environmental challenges and causes toxicity to ecosystems when they leak into aquifers¹⁻³. LNAPLs, which are affected by spills, may either be retained in the vadose zone or infiltrate further down and contaminate groundwater⁴. NAPL-contaminated sites typically have two main zones, i.e., the source zone and the plume zone. The source zone is commonly characterized by the portion of contaminant trapped in the pore space (i.e., residual phase), and by NAPLs which can be transported through a hydraulic gradient (i.e., free-phase)⁵. On the other hand, a small fraction of the NAPLs migrate away from the source zone due to water infiltration and groundwater movement, forming the plume zone, which includes the dissolved, adsorbed, or volatilized constituents along with free phase NAPLs⁶⁻⁸. For example, the lateral spread of BTEX group above the water table is influenced by hydraulic gradients due to its low solubility.

Precise characterization of contamination plumes is critical, and is often achieved through drilling and sampling to directly access contamination. However, these invasive methods provide only point information rather than a continuous distribution of the contaminant plume. Furthermore, drilling and chemical sampling not only are costly, but also increase the risk of vertical spreading of contaminants^{9,10}. In contrast, the geophysical surveys, including ground penetrating radar (GPR)^{11,12}, electrical resistivity (ERT)^{13,14}, and electromagnetic methods (EM)^{15,16} are often cost effective and non-invasive techniques for obtaining continuous information on soil properties over a large area at contaminated sites. Accordingly, electrical or EM methods are promising techniques for detecting LNAPLs in the subsurface, as these substances are electrically insulating and therefore

¹Key Laboratory of Shale Gas and Geoengineering, Institute of Geology and Geophysics, Chinese Academy of Sciences, Beijing 100029, China. ²College of Earth and Planetary Science, University of Chinese Academy of Sciences, Beijing, China. ³School of Environment, Tsinghua University, Beijing 100084, China. ⁴School of Civil Engineering, Shandong University, Jinan 250061, China. ✉email: Tengxiasdu@163.com; maodeqiang@sdu.edu.cn

cause a decrease in conductivity when they replace water in the pore space. The conductivity anomaly caused by LNAPLs mainly depend on the following factors, including type of LNAPLs and release history, plume location, hydrologic processes, biological processes, etc.^{7,17}. Nonetheless, the complex distribution of LNAPLs in soil presents challenges in the field, where the age and degradation state of contaminants can alter groundwater chemistry, i.e., ions are released during biodegradation, or weathering and dissolution of minerals caused by bacteria resulting in organic acids can lead to an increase in groundwater conductivity¹⁸. Thus, relying entirely on electrical conductivity for contaminant characterization might lead to the uncertainty in the delineation of LNAPL extent^{19,20}. For example, the 2D ERT method was used by Godio and Naldi²¹ to identify the low-resistivity anomalies at hydrocarbon contaminants in an industrial site, whereas Rosales et al.²² classified hydrocarbon contaminated soils as high-resistivity anomalies in a former petrol stations survey, underscoring the importance and inclusion of more parameters that should be considered to enhance the interpretation accuracy.

One possible solution to address the limitations of LNAPLs survey with resistivity or conductivity alone is to expand the scope of measurement to include induced polarization (IP). As an extension of resistivity method, IP method can provide information on both the conductive and capacitive properties of the subsurface at the same time, which has a great potential to enable the detection of LNAPLs. Initially, effectiveness of IP in detecting organic contaminants within soils containing clay minerals was observed in the laboratory²³ and field measurements²⁴. The results of Vanhala et al.²⁵ reported that soil and organic mixtures were also polarizable even with low clay mineral content, and extended the applications of IP method in characterizing LNAPL contaminated soil. Slater and Lesmes²⁶ further discussed and summarized the effects of different survey situations on IP data at laboratory and field scales. Recently, several laboratory measurements have demonstrated that the changes in chemical, biological and geological conditions can affect the distribution of LNAPLs within the pores²⁷. Moreover, the sensitivity of IP method to geochemical processes occurring at the pore scale has led to its gradual application in delineating the distribution of contamination plume^{28,29}.

However, conflicting IP results were found for both field and laboratory scale measurements. Some laboratory measurements indicate that the presence of NAPLs typically reduces the IP effect³⁰, while others suggest the opposite³¹. Similarly, contradictory results have also been reported in the field surveys as well. For example, the presence of free-phase NAPLs in an unconfined aquifer has caused a decrease in chargeability⁸, whereas high chargeability has been associated with the signal of LNAPLs in clay in another field investigation³². Consequently, different interpretations have been proposed to explain the IP responses to LNAPL plume^{33,34}. Despite the more frequent use of IP methods in investigating LNAPL contaminated sites, these methods are not as widely used as ERT method. In addition, field scale IP measurements are often complex and challenging due to various factors such as geological background and contaminant compositions³⁵.

This study presents the application of IP method at a former chemical plant to obtain a reliable delineation of LNAPL plume. Field data obtained from time domain IP surveys are analyzed in relation to the interpolation of sampling data. Specifically, two main zones were characterized, including the source zone and the plume zone. Additionally, a comparison between geophysical imaging and the BTEX concentration underscores the validity and rationality of inversion results. Finally, the polarization mechanisms of LNAPLs in source and plume zones are explored based on the IP response characteristics.

Theory of induced polarization

The IP method, also known as complex resistivity or complex conductivity, is based on injecting electric current through a pair of electrodes, while other pairs measure the resulting voltages. The parameters obtained from these measurements reflect the conductive and capacitive properties of the subsurface, with the latter being associated with the polarization of the ions within the electrical double layer (EDL) formed at the interface between fluid and grain²⁶. The EDL is often assumed to consist of two different layers, i.e., the Stern layer and the diffuse layer. The Stern layer is a stationary layer consisting of counter ions on the grain surface, while the diffuse layer consists of ions weakly attracted electrostatically near the grain/water interface³⁶.

Stern layer polarization and membrane polarization are the two main mechanisms that control the low-frequency polarization of metal-free porous media. The Stern layer polarization mechanism is strongly linked to the ion composition and physical properties of soil, such as grain size, ion concentration and the surface charge density of the Stern layer, which have been described in detail in previous work^{26,37,38}. The presence of an additional electric field causes the generation of IP phenomenon by the EDLs, i.e., both the Stern layer and the diffusion layer generate a secondary field in the opposite direction to the electric field, which gradually returns to its original state once the electric field is removed. It is widely accepted that polarization of the Stern layer is much stronger than that of the diffuse layer²⁶. Conversely, the membrane polarization mechanism is associated with the diffuse layer and pore structure, depicting the accumulation of charge at the diffusion layer or pore throats, facilitating the formation of counter-diffusion through the pores³⁹. Our focus in this study is mainly on the Stern layer polarization and membrane polarization, and we examine these mechanisms in conjunction with the IP imaging results in Section "Results and discussion".

IP measurements can be conducted in both frequency and time domains using different equipment, with time domain IP typically utilizing direct current and frequency IP employing alternating current. In frequency domain, the amplitude ($|\sigma|$) and phase (φ) of an alternating current passing through a soil volume are measured. The total complex conductivity σ^* can be calculated as follows:

$$\sigma^*(\omega) = |\sigma|e^{i\varphi} = \sigma' + i\sigma'' \quad (1)$$

where $\omega = 2\pi f$ is angular frequency (rad), f is frequency (Hz), $i = \sqrt{-1}$ represents the pure imaginary number. In addition, $|\sigma|$ is the magnitude of electrical conductivity (S/m), φ is phase (rad), σ' and σ'' are the real and imaginary components (S/m) of the complex conductivity σ^* .

In this study, we will focus on TDIP measurements. In time domain, resistivity or conductivity is measured during the period of current pulse injection. On the other hand, chargeability is recorded when the current is turned off. The intrinsic chargeability m is described as follows⁴¹:

$$m = V_s / V_p, \tag{2}$$

where V_s (V) is the maximum voltage measured immediately after the interruption of the current pulse and V_p (V) is the primary voltage of the transmitted direct current (DC). In fact, chargeability m is usually measured as the integral of the decay curve during a definite time window:

$$m = \frac{1}{V_p} \int_{t_1}^{t_2} V(t) \cdot dt, \tag{3}$$

where $V(t)$ (V) is the residual voltage at time t after the current interruption.

There is a linear correlation between phase φ and chargeability m . Time domain equivalence with the quadrature conductivity σ'' is called normalized chargeability M_n , which is usually calculated to represent the surface chemical characteristics of porous media²⁶. It can be approximately computed by^{40,42}

$$M_n = k \cdot m \cdot |\sigma| \cong \varphi \cdot |\sigma| \cong \varphi \cdot \sigma' \cong \sigma'', \tag{4}$$

where k is the linear coefficient ($k=1.3$)⁴². The normalized chargeability can be calculated from the multiplication of chargeability and conductivity, or the ratio of chargeability to resistivity (Eq. 4).

Field applications frequently involve time-domain IP (TDIP) survey⁴³. In this method, conductivity is measured during the on-time T_{on} , and the secondary voltage decay is recorded during the off-time T_{off} , which is called 50% duty cycle method (Fig. 1b). A limitation of this method is that conductivity and chargeability measurement are conducted for only half of the acquisition time. Advancements in time-domain hardware allows for a faster survey mode with 100% duty cycle method⁴⁴, where the current is injected continuously and the IP responses are also recorded during the on-time T_{on} (Fig. 1a). This advancement substantially increases the signal-to-noise ratio by up to 100% with minimal information loss⁴⁵. Additionally, another pronounced advantage of this survey mode is the reduction of acquisition time by up to 50%, which is mostly preferred for the field surveys.

Mechanistic models have been developed to understand the low and high frequency conductivity of sands^{46,47}. The CPA model is suitable if the phase shift variation is negligible in the induced polarization data⁴⁸. In cases where soils or rocks exhibits little or no frequency-dependent phase shift, a simpler two-parameter CPA model can be used to fit the IP spectrum. The CPA model can be represented as follows:

$$\sigma^*(\omega) = \sigma_n \left(\frac{i\omega}{\omega_0} \right)^b, \tag{5}$$

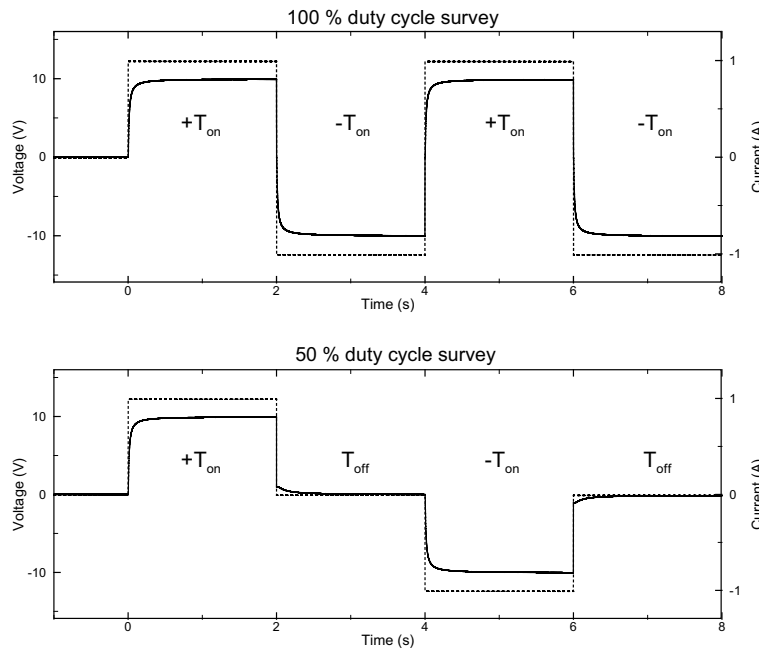


Figure 1. Illustration of 100% duty and 50% duty cycles time-domain induced polarization survey methods. With 100% duty cycle survey, negative current injection period $-T_{on}$ immediately follows the positive current injection $+T_{on}$. In the 50% duty cycle survey, after current injection during T_{on} period, current is turned off during T_{off} period for secondary voltage measurements.

$$\varphi = \frac{\pi}{2} b, \quad (6)$$

where σ_n is the magnitude of the complex conductivity measured at some low frequency ω_0 and b is a parameter describing a power-law dispersion in the spectral response.

Materials and method

The following sub-sections demonstrate information about the study area and previous sampling results in the study region, followed by the geophysical survey conducted to measure IP data.

Field site description

The study site is located in a former chemical plant on the outskirts of Beijing, China. The chemical plant was shut down in 2012, and the original buildings in the plant were all demolished. During its three decades of operation, the investigation site was used for chemical tank storage. Note that several tracks used to transport raw materials across the plant have also been dismantled (see black dashed lines in Fig. 2). Previous geological drilling revealed that the shallow subsurface is predominantly occupied by Quaternary alluvial deposits. These deposits form a shallow unconfined aquifer characterized by four heterogeneous units. The backfill layer extended to 2~4 m below ground surface (bgs) and consisted of silt, sand and gravel materials. Below this layer, it was the main water bearing sandy layer, with occurrence of discontinuous silt and silt clay layers. The main contaminants at the site were characterized as the BTEX group (benzene, ethylbenzene and xylene). The released contaminants are located in this unconfined aquifer, which is confined by a continuous silt clay layer as the bottom impervious boundary at approximately 15~20 m bgs. The water table at this site fluctuated within the range of 2.9~5.2 m bgs. Contour mapping of groundwater levels (Fig. 2) indicated that the overall groundwater flow direction was from southwest to northeast, and the water level at the time of measurement was approximately 5 m bgs.

Previous soil and groundwater sampling

As an integral part of the investigation strategy, both soil and groundwater were sampled to characterize the contamination (see details in Fig. 2). A total of seventeen direct-push boreholes were drilled with Geoprobe, reaching a maximum depth of 6 m. Soil samples were collected from each direct push borehole at 0~2 m bgs and 2 to 6 m bgs, aiming to target the backfill layer and sandy layer, respectively. Apart from the direct push boreholes, two groundwater sampling wells were drilled to a maximum depth of 10 m. Groundwater samples were taken from screen intervals of 8 to 10 m bgs, with soil sampled at 8 m bgs and 10 m bgs during drilling. Samples were collected/processed and analyzed in strict accordance with the relevant standard⁴⁹.

The concentrations dataset of soil and groundwater samples collected from boreholes is presented in Table 1. In general, soil with BTEX concentrations exceeding 180 mg/kg were mainly located in areas encompassing locations S3, S19, S20, S21, S24 and S25 at depth of 2~5 m bgs. The total contaminant concentration ranges from 220.4 mg/kg to 853 mg/kg, with the highest concentration samples collected from S21, and the lowest

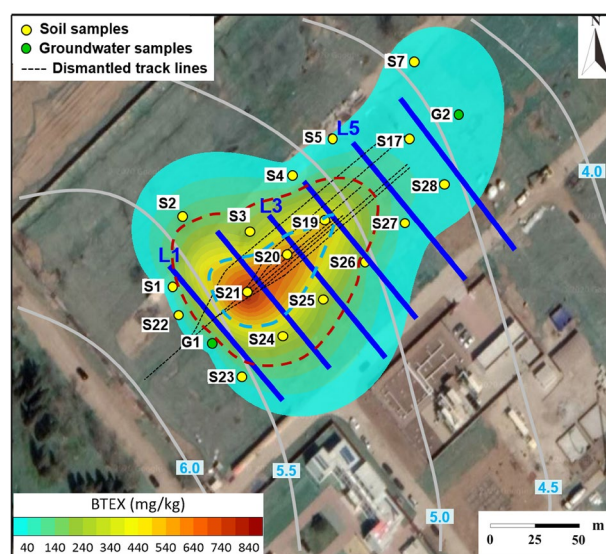


Figure 2. Illustration of field survey and interpolation of contaminant concentration. A total of 14 soil and 2 groundwater samples locations were identified within the survey site. The interpolated BTEX surface indicates the primary area of contamination marked in red dashed line (BTEX concentration ≥ 180 mg/kg). On the other hand, blue dashed line represents the source zone (BTEX concentration ≥ 450 mg/kg). Six time-domain induced polarization survey lines were established, each featuring 32 electrodes with 2 m electrode spacing. The water table in the study region is denoted by solid gray lines and numbers against blue background. In addition, the black dashed lines indicate the dismantled track lines.

Borehole	Depth of collected samples (m bgs)	Benzene	Ethylbenzene	Xylene	Total concentration
S1	0–2	0.2	1.5	5	6.7
	2–6	0.5	2	10	12.5
S2	0–2	2	6	13	21
	2–6	1	5	39	45
S3	0–2	1.6	4.5	21	27.1
	2–6	67	115	50	232
S4	0–2	0.1	1	5	6.1
	2–6	0.3	1	15	16.3
S5	0–1.8	0.1	5	5	10.1
	2–6	0.1	5	6	11.1
S7	0–2	0.1	3	6	9.1
	2–6	0.1	5	5	10.1
S17	0–2	0.6	1	20	21.6
	2–6	0.7	3	10	13.7
S19	0–2	2.3	2	34	38.3
	2–6	164	260	87	511
S20	0–2	2.1	3	45	50.1
	2–6	352	185	138	675
S21	0–2	0.5	4	41	45.5
	2–6	306	361	186	853
S22	0–2	0.5	3	5	8.5
	2–6	0.6	4	4	8.6
S23	0–2	0.6	4	5	9.6
	2–6	0.2	2	31	33.2
S24	0–2	0.5	3	16	19.5
	2–6	44	93	106	243
S25	0–2	3	2	35	58
	2–6	4.4	81	135	220.4
S26	0–2	0.5	3	10	13.5
	2–6	0.4	2	82	84.4
S27	0–2	0.1	2	6	8.1
	2–6	0.1	3	17	20.1
S28	0–2	0.2	2	21	23.2
	2–6	0.1	3	11	14.1
G1	8	0.1	2	3	5.1
G2	10	0.2	1	4	5.2
Threshold values (soil sample)		3	7.2	163	173.2
G1	10	0.1	0.2	0.4	0.7
G2	8	0.1	0.1	0.3	0.5
Threshold values (water samples)		1	0.3	0.5	1.8

Table 1. Concentrations of BTEX group (benzene, ethylbenzene, and xylene) in soil (mg/kg) and groundwater (mg/L) samples. The threshold values are indicated in bold, which are adopted following the relevant standard⁵⁰.

concentration samples obtained from S25. Among these four positions, the highest benzene concentration of 352 mg/kg was recorded in borehole S20, while the lowest was measured in borehole S25 with a concentration of 4.4 mg/kg. For ethylbenzene, the highest concentration of 361 mg/kg was detected in borehole S21, and the lowest concentration of 81 mg/kg was detected in borehole S25. Moreover, excessive xylene was observed only in borehole S21, which had a concentration of 186 mg/kg. In addition, no contaminants were found in soil and groundwater samples collected from boreholes G1 and G2.

TDIP survey

Time-domain induced polarization survey was subsequently conducted on chemical measurements in the same area to improve the accuracy of localizing the contaminant distribution using borehole information. Figure 2 illustrates the deployment of six parallel survey lines with a spacing of 20 m to cover the site. To encompass areas with varying contaminant concentrations, all lines were oriented nearly perpendicular to local groundwater flow direction. Each survey line was equipped with 32 electrodes, spaced 2 m apart. Stainless steel electrodes were

used for both current injection and potential measurements⁴³. A gradient measurement protocol was adopted, resulting in 294 data points per survey line. A 100% duty cycle with 1 s on-time of current injection and 3 full stacks was used for the survey. Data measurements were conducted using ABEM LS2 (www.guidelinegeo.com), where full-wave form polarization data were measured at a sampling rate of 1 kHz. All contact resistances were kept well below 1 k Ω .

Full-wave IP data were inverted with Aarhus workbench⁵¹ by assuming the CPA model⁵². The CPA model is displayed in the form of inversion parameters (σ , φ) and the normalized chargeability (M_n). Every decay curve was processed with the method described by Olsson et al.⁴⁵, and decay curves with all negative chargeability were all discarded. In the end, 274, 269, 248, 256, 259 and 251 data points were retained for the induced polarization inversion, i.e., approximately 88% of the decay curves were retained for each survey line, which indicated a good quality of measured data. Inversion errors were less than 5% for all profiles, with an average pseudodepth of 10 m.

Results and discussion

The subsequent sections include the results from IP inversion representing the delineation of potentially contaminated areas, followed by the integration of IP imaging and chemical results to further delineate the source and plume zones. Finally, we discuss the polarization mechanisms of LNAPLs in different zones based on IP responses.

LNAPL plume characterization with IP images

Prior to the description of IP inversion profiles, the distribution of BTEX is interpolated in Fig. 2, which presents the distributions of total benzene, ethylbenzene and xylene concentrations derived from the soil samples collected at the depths of 2–6 m bgs. Since geophysical methods are not capable of separating contaminant types, the contaminant concentration in this study represents the sum of benzene, ethylbenzene and xylene concentrations, which is similar to findings from previous studies reported by Flores Orozco et al.⁸ and Xia et al.¹³. The interpolation results indicate the areas with BTEX concentration greater than 180 mg/kg, delineated by the red dashed line, which illustrates the main contamination location. Specifically, the area with concentrations greater than 450 mg/kg represents the contaminated source zone (marked by the blue dashed line, e.g., S20 and S21), while the area with lower concentrations (i.e., below 450 mg/kg) represents the plume zone, e.g., S24 and S25. Note that sampling results provide specific information on contaminated site.

Figure 3 shows the inversion results for all six profiles based on the CPA model. The conductivity distribution (Fig. 3a) illustrates that the area above the groundwater table in profiles L1–L4 indicates a low conductivity response of less than 5 mS/m. Figure 3b shows that a high phase layer (> 20 mrad) occupies the shallower subsurface with discontinuities in survey lines L1 to L4. The normalized chargeability shown in Fig. 4c demonstrates the contribution of induced polarization effect to conductivity. Specifically, three survey lines, i.e., L2, L3 and L5, are chosen as examples for detailed analysis, and geological boreholes overlap on the geophysical profile as well. Notably, survey lines L2 and L3 cut through the contaminated zone, while L5 served as a background reference with lower BTEX concentration.

Stratigraphic information obtained from boreholes S21 and S24 close to L2 are consistent, i.e., the vadose zone is mainly composed of backfill, silt and fine sand. However, the IP responses are not identical for different areas with similar geological features. Specifically, a significantly low-conductivity zone (less than 5 mS/m) is observed between depths of 2 and 6 m bgs (Fig. 4a). The intrusion of electrically insulating BTEX leads to a low conductivity response, which is consistent with the sampling results. Although various factors, such as the soil stratum and groundwater level, can affect the electrical response of subsurface media, soil types and moisture content seem to have minimal impacts on conductivity compared to the contaminant intrusion.

At the same depth, the phase continuation is interrupted (Fig. 4b). A lower phase value of less than 20 mrad is marked in the center part by red dashed lines. In contrast, the high phase anomalies above 20 mrad are more evident on the left, as shown by the blue dashed lines (Fig. 4). Interestingly, the corresponding conductivity responses of both areas exhibit low anomalies. The sampling results indicate that these two areas are all contaminated zones, e.g., the BTEX concentration of S21, which corresponds to the red dashed line is 853 mg/kg, while that of S24, which corresponds to the blue dashed line is 243 mg/kg. Therefore, low conductivity accompanied by low phase values signifies a contaminated source zone, while high phase with relatively high conductivity indicates the plume zone. These observations align perfectly with the findings of Johansson et al.⁵³, who reported no obvious phase anomalies in the contaminated source zone, while a relatively strong phase response was detected in the plume area. It is observed that residual free-phase NAPLs could be anticipated from chemical data. This hypothesis is also consistent with measurements from several laboratories^{18,27,33}, suggesting that IP responses are related to the variations in pore properties due to the addition of LNAPLs, and can be explained by the Stern layer polarization or membrane polarization models. Furthermore, normalized chargeability quantifies the magnitude of surface polarization. For porous media comprised of nonmetallic materials, normalized chargeability is related to the characteristics of pore space and surface chemistry, and it can be considered as a direct measurement of the IP effect²⁶. The normalized chargeability (M_n) for the source zone is less than 80 mS/m (marked in orange dashed lines in Fig. 4c), and we speculate that the polarization response significantly decreases due to the high concentration of LNAPLs occupying the pore space within the source zone.

Although conductivity can delineate contaminated areas, it is difficult to distinguish between source and plume zones. This is particularly evident in profile L3 (Fig. 5a). Nevertheless, similar to the results from survey line L2, phase value obtained from time domain IP measurement can be used to effectively distinguish between these two zones. Specifically, phase values less than 20 mrad corresponding to the low conductivity anomalies less than 5 mS/m are divided into two types: phase less than 20 mrad within the red dashed lines, and phase greater than 20 mrad within the blue dashed lines (Fig. 5b). Soil samples taken from boreholes S20 (675 mg/kg) and S25 (220.4 mg/kg)

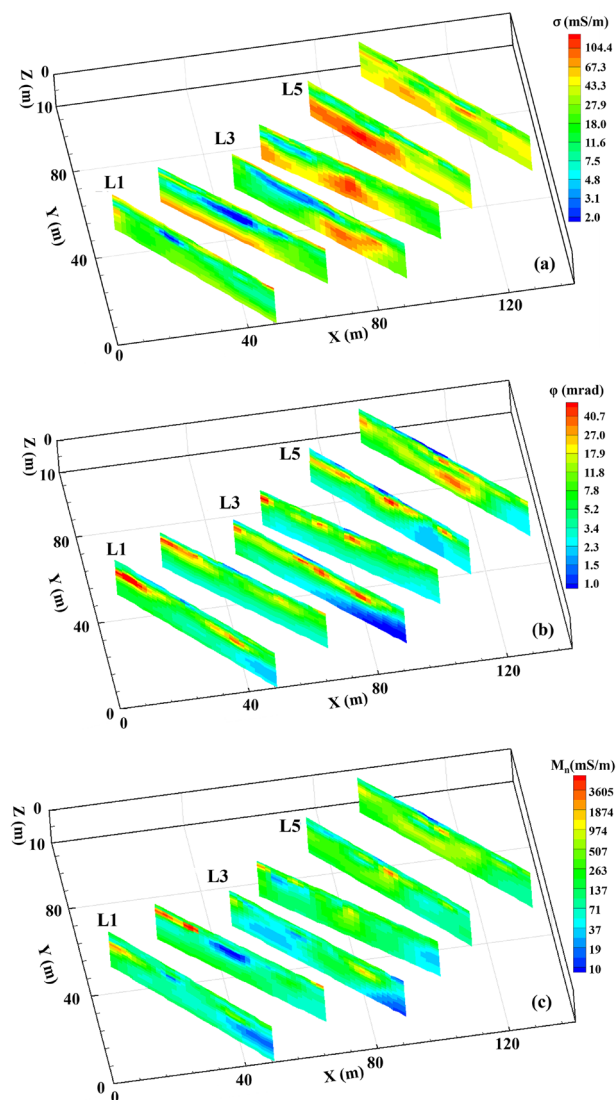


Figure 3. Time-domain distribution of induced polarization results of six profiles; (a) conductivity, (b) phase, and (c) normalized chargeability.

along profile L3, corresponding to the red and blue dashed lines, are classified as the source zone and the plume zone, respectively. Additionally, the normalized chargeability below 80 mS/m marked in orange dashed lines further verifies the decrease of polarization within the source zone and refines the location of source zone (Fig. 5c).

In the non-contaminated area, the conductivity and phase values show a different pattern. The estimated conductivity shows a smooth low magnitude of approximately 8 mS/m, and the conductivity values significantly increase in the region below the water table (Fig. 6a). The estimated phase values are generally high exceeding 20 mrad (Fig. 6b), with no abrupt phase decrease in the profile. Note that the high normalized chargeability anomaly in S27 may be related to the silt layer in the vadose zone. Similar research can be referred to Johansson et al.⁵³ and Revil et al.⁵⁴

As shown in Figs. 4–6, it is difficult to accurately classify the contaminated areas and different zones based on the phase alone. Especially for the plume zones, the phase response of media invaded by small amounts of contaminants may be similar to that of the clean silt layer, such as the high phase anomaly (>20 mrad) shown in profiles L3 and L5. Nevertheless, changes in conductivity response due to contaminant intrusion are more pronounced than differences in geological factors, i.e., the conductivity response (<5 mS/m) is similar in areas with different geological features but similar contaminant concentrations (>180 mg/kg). Therefore, to accurately classify the contaminated areas and different zones, the phase distribution must be analyzed in combination with conductivity.

Comparison between geophysical imaging and concentration measurements

In this section, we use the estimated induced polarization parameters to mark the scope of the LNAPL contaminated area. Figure 7 indicates the scatter plots between BTEX concentrations and IP parameters extracted from

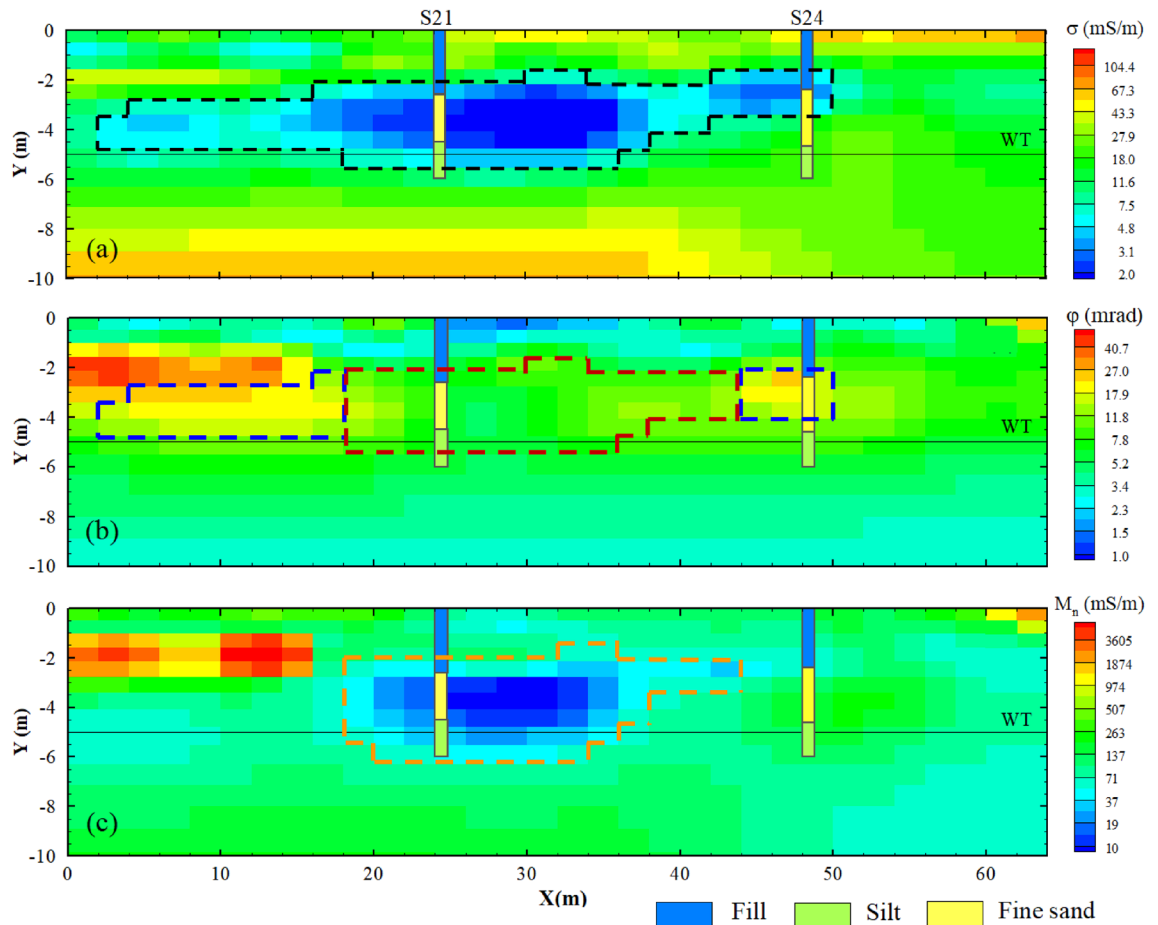


Figure 4. Inversion results of LNAPL contaminant in profile L2; (a) conductivity, (b) phase, (c) normalized chargeability. The black solid lines represent the position of water table. The low conductivity anomaly (< 5 mS/m) marked in black dashed lines indicates the contaminated area consistent with the sampling data. The phase values corresponding to the high resistance anomaly are divided into the source zone marked in red dashed lines (< 20 mrad) and the plume zone marked in blue dashed lines (> 20 mrad). Moreover, the normalized chargeability below 80 mS/m marked in orange dashed lines represents the decrease of polarization within the source zone.

profiles L1–L6. Note that the geophysical data are taken from average cell values at depths of 2–6 m bgs close to the boreholes. Figure 7a indicates the results for 13 boreholes at depths of 2–6 m bgs (S1, S3, S17, S19, S20, S21, S22, S23, S24, S25, S26, S27 and S28 shown in Fig. 2) versus IP parameters, while Fig. 7b,c show the results for 6 boreholes (S3, S19, S20, S21, S24 and S25) within the contaminated area versus IP parameters. The samples analysis segregates conductivity into two distinct regions, i.e., non-contaminated area and contaminated area (Fig. 7a). In particular, the conductivity values at the sampling points corresponding to the BTEX concentrations exceeding 180 mg/kg are below 5 mS/m. Therefore, the threshold conductivity is identified based on the relationship between BTEX concentration and conductivity, which is 5 mS/m. However, it is challenging to distinguish between the source zone and plume zone within contaminated area based solely on conductivity. For example, the conductivity corresponding to source zone with BTEX of 675 mg/kg is 2.62 mS/m, while the conductivity corresponding to plume zone with BTEX of 243 mg/kg is 2.57 mS/m, thus the two zones cannot be effectively distinguished by conductivity alone.

However, a noticeable difference in phase between the source zone and plume zone is observed (Fig. 7b). Within the contaminated area, there is a linear negative relationship between BTEX and phase (slope < 0 , $R^2 = 0.76$), where a plume zone with a low concentration corresponds to a high phase, while a source zone with a high concentration corresponds to a low phase. The threshold phase value corresponding to the critical concentration (450 mg/kg) is 20 mrad. In addition, the normalized chargeability threshold for contaminated source zone is 80 mS/m. Since normalized parameters are more sensitive to the chemical properties of material surface compared to conductivity and phase, the difference in normalized chargeability between these two zones is more evident. Specifically, the maximum difference in phase between plume and source zones is ~ 20 mrad, which varies by $\sim 65\%$ ((max-min)/max), correspondingly, the maximum difference in normalized chargeability is ~ 150 mS/m, which varies by $\sim 93\%$. On the other hand, the slope of decreasing fit line in Fig. 7c (-0.2) is smaller than the value in Fig. 7b (-0.03), which demonstrates a more distinct difference in the normalized chargeability corresponding to the two zones. Nevertheless, the correlation coefficient of the linear fit between

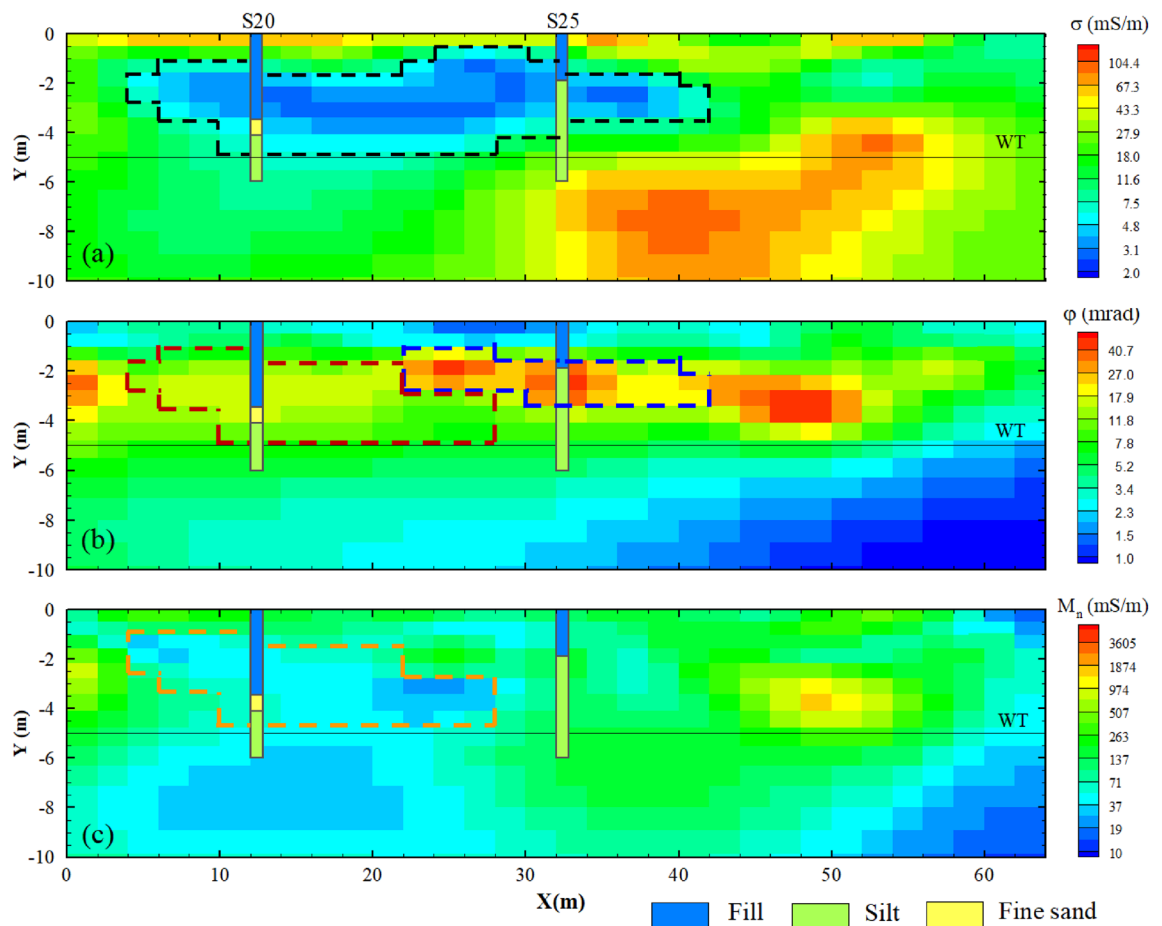


Figure 5. Inversion results of LNAPL contaminated in profile L3; (a) conductivity, (b) phase, (c) normalized chargeability. Legends and description are the same as those in Fig. 4.

BTEX concentration and normalized chargeability (0.88) is greater than that of phase (0.76). Accordingly, as mentioned above, the relationship between IP parameters and BTEX further emphasizes the rationality of inversion results for zone delineation and interpretation. Note that we focused primarily on IP effects in the source and plume zones within the contaminated area delineated by the conductivity distribution, rather than comparing the differences in IP effects between the plume zone and the uncontaminated area. For the contaminated area, the IP effect is significantly greater in the plume zone than that in the source zone, which is verified by the BTEX concentration from the borehole sampling.

A similar numerical simulation study was conducted by Almpanis et al.⁵⁵, who developed a novel DNAPL-DCIP numerical model and calculated the corresponding resistivity and chargeability responses. The simulation results illustrated that the resistivity distribution effectively delineated the DNAPL source zone, while the chargeability and normalized chargeability distributions accurately delineated the soil variability. It is worth mentioning that in contrast to results from the ideal numerical modelling conditions, the variations in IP response within contaminated area in this study are hypothesized not to be caused by variations in soil but rather by the different geometrical configuration of LNAPL in the pore space. This can be verified from the strata information and contaminant concentration results obtained from the boreholes. For example, despite the consistency in strata information obtained from S21 and S24, the BTEX concentrations measured at these two locations differ and, consequently result in distinct IP responses (M_n and ϕ) as shown in Fig. 4.

Moreover, based on the chemical sampling analysis, LNAPLs were mainly distributed at depths between 2 m bgs and 6 m bgs, and the averaged geophysical results of six profiles are shown in Fig. 8. The black dashed line with conductivity values less than 5 mS/m reflects the contaminated area (Fig. 8a). The contaminated source zone, characterized by a normalized chargeability less than 80 mS/m and a corresponding phase value less than 20 mrad, is marked by an orange dashed line, (Fig. 8b,c). Sampling points with BTEX concentrations above 450 mg/kg are within the orange dashed lines indicating the source zone, while sampling points with BTEX concentrations above 180 mg/kg are enclosed by the black dashed lines representing the contaminated area.

Geophysical survey and borehole sampling have distinct requirements for information collection, and can complement and validate each other effectively. Figure 9 demonstrates the difference between interpolation results of geophysical data and interpolation results of chemical sampling analysis. It should be noted that the geophysical results present a more accurate delineation of contaminated area (black dashed lines) than the interpolation (red dashed lines) from the chemical sampling information alone. On the other hand, the characterized

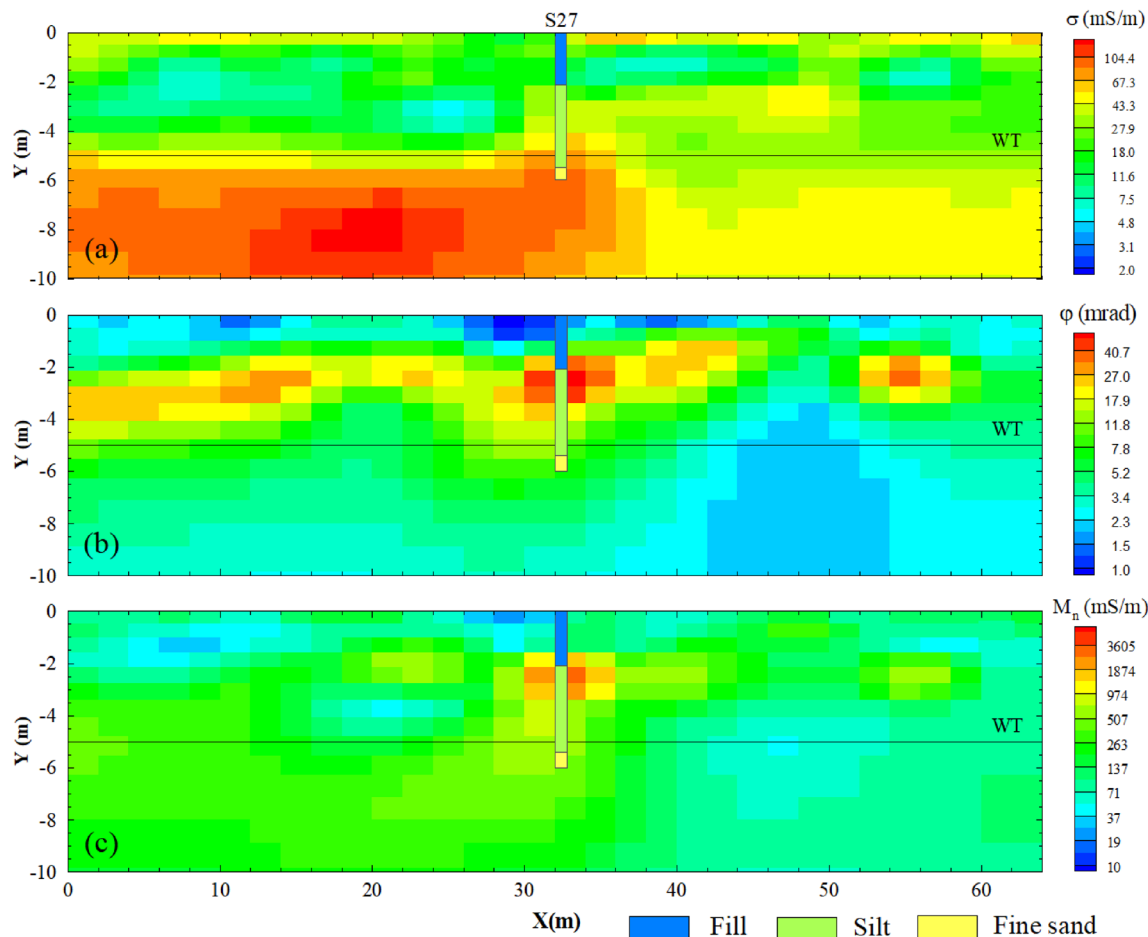


Figure 6. Inversion results of non-contaminated in profile L5; (a) conductivity, (b) phase, (c) normalized chargeability. Legends are the same as those in Fig. 4.

source zone based on IP parameters has a different shape and appears to be larger than that inferred from sampling interpolation. The continuous information on the source or plume zone within the contaminated area from geophysical surveys seems to be more convincing than the limited point concentrations from boreholes. However, it is challenging to design the location of the survey lines rationally without prior sampling information. Therefore, a good balance between these two methods facilitates the acquisition of accurate information on the delineation of contaminated zones.

In addition, by utilizing prior information of the contaminated site, contamination release history is confirmed through the utilization of IP imaging representations. By integrating contaminant and stratum information obtained from boreholes, the anomalies measured on L1-L4 delineate a continuous layer with low conductivity and normalized chargeability, indicating potential contamination originated from multiple locations. No buildings have ever existed on the site other than the tracks used to transport raw materials. Therefore, subsurface contamination may be attributed to the leakage of raw material at rail tracks interchange during transportation.

Induced polarization between plume and source zones

Our results demonstrate that the variations of phase and normalized chargeability related to the BTEX concentration changes are significantly greater than those in conductivity for the contaminated area. The concentration and distribution of LNAPLs in pore space are critical because they can change the micro geometrical characteristics at the pore scale and the current paths through the soil.

For the plume zone where the soil is unsaturated with LNAPLs, there are several possible distributions of free-phase LNAPLs. The distribution of free-phase products within pore space is controlled by the physical characteristics of NAPL (e.g., density and viscosity), and the non-homogeneity of the aquifer parameters (e.g., permeability and storage coefficients)⁵⁶. In this study, IP response in the plume zone exhibit enhanced polarization characteristics, e.g., phase > 20 mrad or normalized chargeability > 80 mS/m. We focus on the conceptual model in which LNAPLs are present as isolated spheres within the plume zone⁵³, indicating that small droplets are confined to specific soil pores (Fig. 10). This conceptual model of plume zone is similar to the water-wet distribution of LNAPLs in the pore space described by Schmutz et al.³³ and Revil et al.¹⁸. The increased phase can be attributed to the Stern layer or membrane polarization. Specifically, the intrusion of LNAPL leading to the formation of a water–oil interface within the medium, attracting counter ions similar to the EDL formed at the

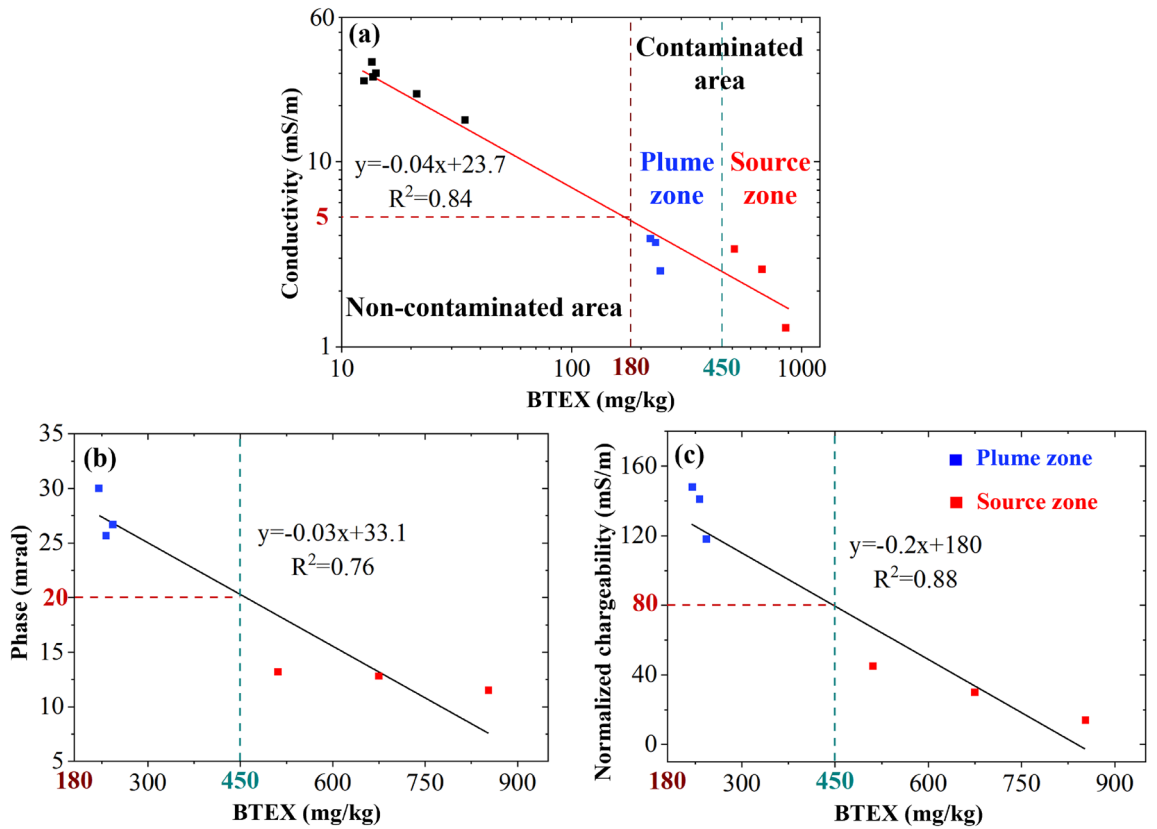


Figure 7. BTEX as a function of (a) conductivity, (b) phase, (c) normalized chargeability. Although the conductivity is linearly related to BTEX, the plume and source zones within the contaminated area cannot be directly distinguished. For contaminated area, the maximum difference in phase between plume and source zones is 20 mrad (~65%), while the maximum difference in normalized chargeability between two zones is more evident (~93%, ~150 mS/m).

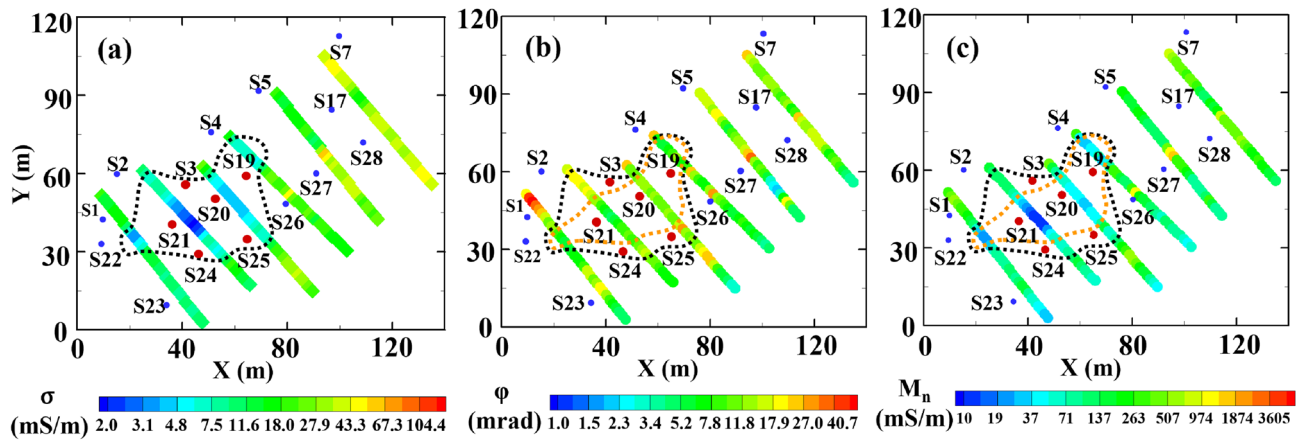


Figure 8. Averaged inversion results between 2 m bgs to 6 m bgs for all six profiles in (a) conductivity, (b) phase, (c) normalized chargeability. Conductivity less 5 mS/m interprets contaminated area enclosed with black dashed lines, and orange dashed lines indicate source zone with normalized chargeability below 80 mS/m, which corresponds to a phase below 20 mrad. The red dots represent the contaminated sampling locations between 2 m bgs to 6 m bgs, and the blue dots represent non-contaminated sampling locations.

soil grain-water interface, thus enhancing the IP response of the soil system through the formation of a polarizable EDL⁵⁷. On the other hand, according to the membrane polarization, the pore space between particles and LNAPLs droplets can be defined as the ion-selective zone, while pore throat constitutes the non-selective zone, i.e., in contrast to the case of uncontaminated media, the pore throat constitutes the selective zone and the non-selective zone consists of pores. A similar process has been described by Titov et al.⁵⁷. Polarization is enhanced in the presence of LNAPLs as the ion transparency between these zones increases⁵³.

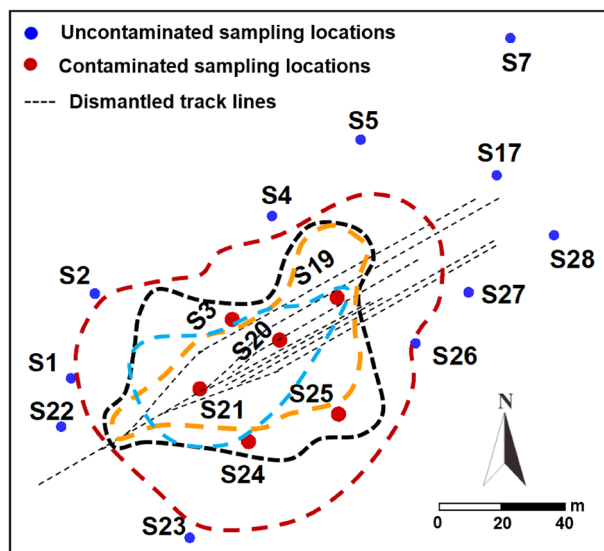


Figure 9. Delineation of contaminated areas based on geophysical data. Readers are referred to Fig. 2 and Fig. 8 for the descriptions of red and blue dashed lines, and black and orange lines, respectively.

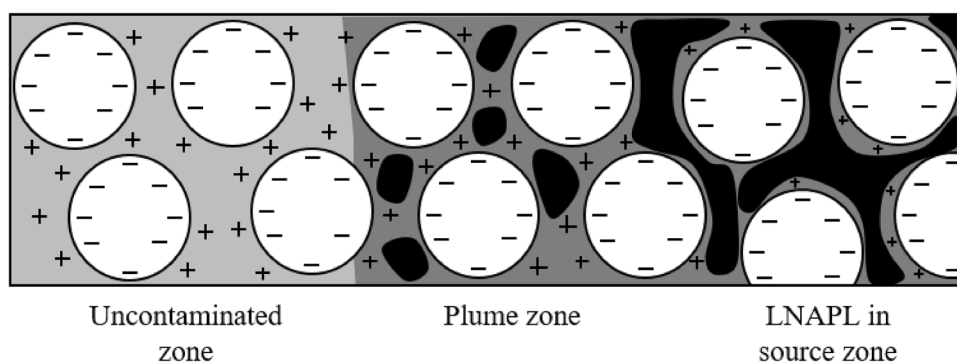


Figure 10. Illustration of LNAPL distributions in pore spaces (modified from Flores Orozco et al.⁸). In source zone with high contaminant concentration, LNAPLs are arranged as a continuous phase in the pore space. With lower concentration next to source zone, residual LNAPL droplets exist in pore space. There is still a complete formation of electrical double layer on the grain surface. In most cases, the decrease in IP effect is due to the free-phase products replacing the pore water required for the formation of the EDLs in which the polarization occurs.

In contrast, laboratory measurements by Shefer et al.³⁴ indicated that the imaginary conductivity decreased for decane contaminated soil under variably saturated conditions. In his hypothesis, the addition of decane may have changed the position or size of anion/cation selective zones, thus causing a variation in the concentration gradient and a decrease in polarization. However, comparing results from previous laboratory measurements is not always straightforward, as there may be differences in experimental conditions and types of NAPLs⁵⁸. Moreover, under field site condition, residual LNAPLs within soil pores are not all formed in a certain way, i.e., one or more combinations of polarization mechanisms determine the polarization response.

When the soil is predominantly saturated with LNAPLs, such as in the contaminated source zone shown in Fig. 10, there is an interconnected condition in the pore space, with a continuous distribution of LNAPLs. The conceptual model of source zone is similar to the arrangement of NAPL in nearly fully saturated pore space reported by Johansson et al.⁵³. Regardless of the extent of saturation, for source zone with high LNAPLs concentration, insulated LNAPLs that completely occupy soil pores usually prevent current injection into the porous medium and lead to the absence of EDLs, making it impossible to obtain IP responses. The decrease in phase response is mainly attributed to the suppression of membrane and Stern layer polarization caused by the substitution of pore water with LNAPLs. Similar results were reported by Cassiani et al.⁵⁸ and Schmutz et al.³³, where experimental measurements of low clay sediments showed that the IP effect decreases with increasing oil content. Consequently, performing IP measurements under field conditions may reveal, a decrease in electrical conductivity (< 5 mS/m) and a decrease in phase responses (< 20 mrad for phase or < 80 mS/m for normalized chargeability) in the source zone within contaminated area.

Overall, the field results in this study show that source zone with high BTEX concentrations in soil correspond to low IP responses, while plume zone with low concentrations enhance IP effect. Similarly, Flores Orozco et al.⁸ observed that the IP effects (M_n and φ) increase with increasing BTEX concentration below saturation concentration (< 1.7 g/L), while the polarization responses (M_n and φ) show a decreasing trend when the BTEX concentration is higher than the saturation concentration (> 1.7 g/L), which may be caused by the presence of free-phase products replacing pore water.

Conclusions

This study illustrates a typical approach for investigating LNAPLs contamination by employing the induced polarization (IP) imaging method at a former chemical plant. The results illustrate that the variations in phase and normalized chargeability caused by BTEX can be used to effectively distinguish between the source and plume zones within the contaminated area delineated by conductivity.

The interpolation of sampling data indicates that the area with BTEX concentrations exceeding 450 mg/kg represents the source zone within contaminated area. Moreover, IP measurements aid in comprehending the distribution of LNAPLs. The results show that the threshold conductivity value of 5 mS/m defined by the relationship between BTEX concentration and conductivity represent the contaminated area. Although conductivity can delineate the contaminated area, it is difficult to distinguish the source zone from the plume zone. However, phase corresponding to the low conductivity anomaly are divided into two zones, i.e., source and plume zones, which is consistent with the sampling information. Specifically, the threshold phase value corresponding to the critical concentration (450 mg/kg) is 20 mrad. Furthermore, the normalized chargeability below 80 mS/m further verifies the suppression of polarization within source zone and refines the location of source zone. Consequently, geophysical results present a more accurate delineation of contaminated area than the interpolation from the sampling information alone.

Field results further demonstrate that source zone with high BTEX in soil correspond to low IP responses, while plume zone with low concentrations enhance IP effect. In unsaturated soil with LNAPLs within the plume zone, the increased phase may be attributed to the Stern layer or membrane polarization. Despite the different results in previous studies, the enhanced IP response in this case is related to the combination of multiple polarization mechanisms. In the source zone where the soil is essentially saturated with LNAPLs, the insulated LNAPLs fully occupy the pores, which usually leads to the absence of EDLs, resulting in a low phase in the source zone. The different IP responses in two zones is attributed to the concentration and distribution of LNAPLs within the pore space. Overall, this study suggests that IP is a valuable tool for mapping and characterizing different LNAPLs contaminated zones, and can facilitate the optimization of drillings and monitoring wells for further site assessment and remediation.

Data availability

Data will be made available on request (Teng Xia, Tengxiasdu@163.com; Deqiang Mao, maodeqiang@sdu.edu.cn).

Received: 19 January 2024; Accepted: 3 July 2024

Published online: 06 August 2024

References

- Mayer, A. & Hassanizadeh, S.M. Soil and Groundwater Contamination: Nonaqueous Phase Liquids—Principles and Observations (ed. Mayer, A., Hassanizadeh, S. M.) 47–95 (American Geophysical Union, 2005).
- Fitts, C.R. Groundwater Science (Second Edition) (ed. Fitts, C. R.) 499–585 (Academic Press, 2013).
- Yang, C. G., Offiong, N. A., Zhang, C. P., Liu, F. Y. & Dong, J. Mechanisms of irreversible density modification using colloidal biliquid aphron for dense nonaqueous phase liquids in contaminated aquifer remediation. *J. Hazard. Mater.* **415**, 125667 (2021).
- Halihan, T., Sefa, V., Sale, T. & Lyverse, M. Mechanism for detecting NAPL using electrical resistivity imaging. *J. Contam. Hydrol.* **205**, 57–69 (2017).
- Kueper, B.H. et al. An illustrated handbook of DNAPL transport and fate in the subsurface. Environmental Agency R&D Publication 133. Environmental Agency, U.K. (2003).
- Sauck, W. A. A model for the resistivity structure of LNAPL plumes and their environs in sandy sediments. *J. Appl. Geophys.* **44**, 151–165 (2000).
- Atekwana, E. A. & Atekwana, E. A. Geophysical signatures of microbial activity at hydrocarbon contaminated sites: a review. *Surv. Geophys.* **31**, 247–283 (2010).
- Flores Orozco, A. et al. Delineation of subsurface hydrocarbon contamination at a former hydrogenation plant using spectral induced polarization imaging. *J. Contam. Hydrol.* **136**, 131–144 (2012).
- Soga, K., Page, J. W. E. & Illangasekare, T. H. A review of NAPL source zone remediation efficiency and the mass flux approach. *J. Hazard. Mater.* **110**, 13–27 (2004).
- Schädler, S., Morio, M., Bartke, S. & Finkel, M. Integrated planning and spatial evaluation of megasite remediation and reuse options. *J. Contam. Hydrol.* **127**, 88–100 (2012).
- Orlando, L. Detection and analysis of LNAPL using the instantaneous amplitude and frequency of ground-penetrating radar data. *Geophys. Prospect.* **50**(1), 27–41 (2002).
- Cassidy, N. J. GPR attenuation and scattering in a mature hydrocarbon spill: a modeling study. *Vadose. Zone. J.* **7**, 140–159 (2008).
- Xia, T., Dong, Y., Mao, D. & Meng, J. Delineation of LNAPL contaminant plumes at a former perfumery plant using electrical resistivity tomography. *Hydrogeol. J.* **29**(3), 1189–1201 (2021).
- Meng, J. et al. Detailed LNAPL plume mapping using electrical resistivity tomography inside an industrial building. *Acta Geophysica.* **70**, 1651–1663 (2022).
- Abbaspour, K., Matta, V., Huggenberger, P. & Johnson, C. A. A contaminated site investigation: comparison of information gained from geophysical measurements and hydrogeological medeling. *J. Contam. Hydrol.* **40**, 365–380 (2000).
- Tezkan, B., Georgescu, P. & Fauzi, U. A radiomagnetotelluric survey on an oil-contaminated area near the Brazi Refinery. *Romania. Geophys. Prospect.* **53**(3), 311–323 (2005).

17. Benson, A. K., Payne, K. L. & Stubben, M. A. Mapping groundwater contamination using dc resistivity and VLF geophysical methods—A case study. *Geophysics*. **62**, 80–86 (1997).
18. Revil, A., Schmutz, M. & Batzle, M. L. Influence of oil wettability upon spectral induced polarization of oil-bearing sands. *Geophysics*. **76**(5), A31–A36 (2011).
19. Gazoty, A. *et al.* Application of time domain induced polarization to the mapping of lithotypes in a landfill site. *Hydrol. Earth. Syst. Sc.* **16**(6), 1793–1804 (2012).
20. Wu, Y. X., Hubbard, S. & Wellman, D. Geophysical monitoring of foam used to deliver remediation treatments within the vadose zone. *Vadose. Zone. J.* **11**(4), 280–288 (2012).
21. Godio, A. & Naldi, M. Two-dimensional electrical imaging for detection of hydrocarbon contaminants. *Near. Surf. Geophys.* **1**(3), 131–137 (2003).
22. Rosales, R. M., Martínez-Pagan, P., Faz, A. & Moreno-Correo, M. Environmental monitoring using electrical resistivity tomography (ERT) in the subsoil of three former petrol stations in SE of Spain. *Water. Air. Soil. Pollut.* **223**, 3757–3773 (2012).
23. Olhoeft, G. R. Low-frequency electrical properties. *Geophysics*. **50**, 2492–2503 (1985).
24. Towle, J. N. Direct detection of hydrocarbon contaminants using the induced-polarization method. *SEG Tech. Program Expand. Abstr.* **4**(1), 446–446 (1985).
25. Vanhala, H., Soininen, H. & Kukkonen, I. Detecting organic chemical contaminants by spectral-induced polarization method in glacial till environment. *Geophysics*. **57**(8), 1014–1017 (1992).
26. Slater, L. & Lesmes, D. P. IP interpretation in environmental investigations. *Geophysics*. **67**(1), 77–88 (2002).
27. Martinho, E., Almeida, F. & Matias, M. S. An experimental study of organic pollutant effects on time domain induced polarization measurements. *J. Appl. Geophys.* **60**(1), 27–40 (2006).
28. Blondel, A., Schmutz, M., Franceschi, M., Tichané, F. & Carles, M. Temporal evolution of the geoelectrical response on a hydrocarbon contaminated site. *J. Appl. Geophys.* **103**, 161–171 (2014).
29. Castelluccio, M. *et al.* Using a multi-method approach based on soil radon deficit, resistivity, and induced polarization measurements to monitor non-aqueous phase liquid contamination in two study areas in Italy and India. *Environ. Sci. Pollut. R.* **25**, 12515–12527 (2018).
30. Chambers, J. E., Loke, M. H., Ogilvy, R. D. & Meldrum, P. I. Non-invasive monitoring of DNAPL migration through a saturated porous medium using electrical impedance tomography. *J. Contam. Hydrol.* **68**, 1–22 (2004).
31. Schmutz, M., Blondel, A. & Revil, A. Saturation dependence of the quadrature conductivity of oil-bearing sands. *Geophys. Res. Lett.* **39**(3), L03402 (2012).
32. Deceuster, J. & Kaufmann, O. Improving the delineation of hydrocarbon-impacted soils and water through induced polarization (IP) tomographies: a field study at an industrial waste land. *J. Contam. Hydrol.* **136–137**, 25–42 (2012).
33. Schmutz, M. *et al.* Influence of oil saturation upon spectral induced polarization of oil-bearing sands. *Geophys. J. Int.* **183**(1), 211–224 (2010).
34. Shefer, I., Schwartz, N. & Furman, A. The effect of free-phase NAPL on the spectral induced polarization signature of variably saturated soil. *Water. Resour. Res.* **49**(10), 6229–6237 (2013).
35. Flores Orozco, A., Gallistl, J., Steiner, M., Brandstätter, C. & Fellner, J. Mapping biogeochemically active zones in landfills with induced polarization imaging: The Heferlbach landfill. *Waste Manag.* **107**, 121–132 (2020).
36. Revil, A. Spectral induced polarization of shaly sands: Influence of the electrical double layer. *Water Resour. Res.* **48**, W02517 (2012).
37. Bücker, M., Flores Orozco, A., Undorf, S. & Kemna, A. On the role of stern- and diffuse-layer polarization mechanisms in porous media. *J. Geophys. Res. Solid Earth.* **124**, 5656–5677 (2019).
38. Binley, A. & Slater, L. *Electrical Properties of the Near-Surface Earth. In: Resistivity and Induced Polarization: Theory and Applications to the Near-Surface Earth.* Cambridge: Cambridge University Press. 18–99 (2020)
39. Revil, A. & Florsch, N. Determination of permeability from spectral induced polarization in granular media. *Geophys. J. Int.* **181**, 1480–1498 (2010).
40. Mao, D., Revil, A. & Hinton, J. Induced polarization response of porous media with metallic particles—Part 4. Detection of metallic and nonmetallic targets in time-domain-induced polarization tomography. *Geophysics*. **81**(4), D359–375 (2016).
41. Seigel, H. O. Mathematical formulation and type curves for induced polarization. *Geophysics*. **24**(3), 547–565 (1959).
42. Mwakanyamale, K., Slater, L., Binley, A. & Ntarlagiannis, D. Lithologic imaging using complex conductivity: Lessons learned from the Hanford 300 Area. *Geophysics* **77**(6), 397–E409 (2012).
43. Dahlin, T., Leroux, V. & Nissen, J. Measuring techniques in induced polarization imaging. *J. Appl. Geophys.* **50**(3), 279–298 (2002).
44. Dahlin, T. & Leroux, V. Improvement in time-domain induced polarization data quality with multi-electrode systems by separating current and potential cables. *Near Surf. Geophys.* **10**, 545–656 (2012).
45. Olsson, P., Dahlin, T., Fiandaca, G. & Auken, E. Measuring time-domain spectral induced polarization in the on-time: Decreasing acquisition time and increasing signal-to-noise ratio. *J. Appl. Geophys.* **123**, 316–321 (2015).
46. Revil, A. On charge accumulations in heterogeneous porous materials under the influence of an electrical field. *Geophysics*. **78**(4), D271–D291 (2013).
47. Revil, A. Effective conductivity and permittivity of unsaturated porous materials in the frequency range 1 MHz–1 GHz. *Water Resour. Res.* **49**, 306–327 (2013).
48. Fiandaca, G., Auken, E. & Christiansen, A.V. Advances in spectral inversion of time-domain induced polarization, in *Proceedings of the 4th International Workshop on Induced Polarization*, Aarhus, Denmark. (2016).
49. China Geological Survey. Geological survey and evaluation standards for soil and groundwater in contaminated sites. DD 2014–06. <http://www.cgs.gov.cn/upload/201501/20150105/20150327112909776.pdf>. (2014).
50. Ministry of Ecology and Environment of the People's Republic of China. Environmental quality standards for surface water. GB 3838–2002. China Environmental Science Press. <https://www.mee.gov.cn/ywgz/fgbz/bzwb/shjbjh/shjzlbz/200206/W020061027509896672057.pdf>. (2002).
51. Auken, E., Viezzoli, A. & Christensen, A. A single software for processing, inversion, and presentation of AEM data of different systems: The Aarhus workbench. *ASEG Extended Abstracts*. <https://doi.org/10.1071/aseg2009ab062> (2009).
52. Fiandaca, G. *et al.* Resolving spectral information from time domain induced polarization data through 2-D inversion. *Geophys. J. Int.* **192**(2), 631–646 (2013).
53. Johansson, S., Fiandaca, G. & Dahlin, T. Influence of non-aqueous phase liquid configuration on induced polarization parameters: Conceptual models applied to a time-domain field case study. *J. Appl. Geophys.* **123**, 295–309 (2015).
54. Revil, A. *et al.* Field-scale estimation of soil properties from spectral induced polarization tomography. *Geoderma*. **403**, 115380 (2021).
55. Almpanis, A., Gerhard, J. & Power, C. Mapping and monitoring of DNAPL source zones with combined direct current resistivity and induced polarization: A field-scale numerical investigation. *Water Resour. Res.* **57**(11), e202WR1031366 (2021).
56. Zhou, Y. Q. & Cardiff, M. Oscillatory hydraulic testing as a strategy for NAPL source zone monitoring: Laboratory experiments. *J. Contam. Hydrol.* **200**, 24–34 (2017).
57. Titov, K., Kemna, A., Tarasov, A. & Vereecken, H. Induced polarization of unsaturated sands determined through time domain measurements. *Vadose. Zone. J.* **3**(4), 1160–1168 (2004).

58. Cassiani, G., Kemna, A., Villa, A. & Zimmermann, E. Spectral induced polarization for the characterization of free-phase hydrocarbon contamination of sediments with low clay content. *Near Surf. Geophys.* 7(5–6), 547–562 (2009).

Acknowledgements

The support from the National Engineering Laboratory for Site Remediation Technologies is appreciated by the first author (No. NEL-SRT201906). The corresponding author would like to thank the support of Natural Science Foundation (42177056) and Shandong National Science Foundation (ZR2019MEE109).

Author contributions

Y.D.: Methodology, Resources—review & editing, Funding acquisition. T.X.: Conceptualization, Methodology, Formal analysis, Writing—original draft. J.M.: Writing—review & editing. D.M.: Conceptualization, Resources, Writing—review & editing, Funding acquisition.

Competing interests

The authors declare no competing interests.

Additional information

Correspondence and requests for materials should be addressed to T.X. or D.M.

Reprints and permissions information is available at www.nature.com/reprints.

Publisher's note Springer Nature remains neutral with regard to jurisdictional claims in published maps and institutional affiliations.

Open Access This article is licensed under a Creative Commons Attribution-NonCommercial-NoDerivatives 4.0 International License, which permits any non-commercial use, sharing, distribution and reproduction in any medium or format, as long as you give appropriate credit to the original author(s) and the source, provide a link to the Creative Commons licence, and indicate if you modified the licensed material. You do not have permission under this licence to share adapted material derived from this article or parts of it. The images or other third party material in this article are included in the article's Creative Commons licence, unless indicated otherwise in a credit line to the material. If material is not included in the article's Creative Commons licence and your intended use is not permitted by statutory regulation or exceeds the permitted use, you will need to obtain permission directly from the copyright holder. To view a copy of this licence, visit <http://creativecommons.org/licenses/by-nc-nd/4.0/>.

© The Author(s) 2024